AFRL-AFOSR-UK-TR-2022-0115

Advanced surface artificial materials for high power microwave sources

Phelps, Alan
UNIVERSITY OF STRATHCLYDE VIZ ROYAL COLLEGE OF SCIENCE & TECHNOLOGY
MCCANCE BUILDING
GLASGOW, LANARKSHIRE, G1 1XQ
GBR

09/01/2022
Final Technical Report

Air Force Research Laboratory
Air Force Office of Scientific Research
European Office of Aerospace Research and Development
Unit 4515 Box 14, APO AE 09421

REPORT DOCUMENTATION PAGE

PLEASE DO NOT RETURN YOUR FORM TO THE ABOVE ORGANIZATION.

1. REPORT DATE	2. REPORT TYPE	3. DATES COVERED	
		START DATE	END DATE
20220901	Final	20170415	20220414

4. TITLE AND SUBTITLE
Advanced surface artificial materials for high power microwave sources

5a. CONTRACT NUMBER	5b. GRANT NUMBER	5c. PROGRAM ELEMENT NUMBER
	FA9550-17-1-0095	61102F
5d. PROJECT NUMBER	**5e. TASK NUMBER**	**5f. WORK UNIT NUMBER**

6. AUTHOR(S)
Alan Phelps

7. PERFORMING ORGANIZATION NAME(S) AND ADDRESS(ES)
UNIVERSITY OF STRATHCLYDE VIZ ROYAL COLLEGE OF SCIENCE & TECHNOLOGY
MCCANCE BUILDING
GLASGOW, LANARKSHIRE G1 1XQ
GBR

8. PERFORMING ORGANIZATION REPORT NUMBER

9. SPONSORING/MONITORING AGENCY NAME(S) AND ADDRESS(ES)	10. SPONSOR/MONITOR'S ACRONYM(S)	11. SPONSOR/MONITOR'S REPORT NUMBER(S)
EOARD UNIT 4515 APO AE 09421-4515	AFRL/AFOSR IOE	AFRL-AFOSR-UK-TR-2022-0115

12. DISTRIBUTION/AVAILABILITY STATEMENT
A Distribution Unlimited: PB Public Release

13. SUPPLEMENTARY NOTES

14. ABSTRACT
Research results are reported of advanced cylindrical surface two-dimensional periodic surface lattice (2D PSL) structures for applications in high power microwave sources. 2D PSL structures enable highly overmoded sources to emit coherently at higher powers than conventional sources. The principle is independent of frequency from a few GHz up to THz frequencies. This research has produced several publications.
Analytical theory, combined with numerical modeling, has revealed several very promising new research routes. Recent results have highlighted the potential for higher performance 2D PSL sources using electron beams produced by advanced carbon
nanotube cathodes. Exciting new research opportunities include phase locking of multiple 2D PSL oscillators, achieving superradiant 2D PSL sources and exploring the potential for powerful 2D PSL amplifiers. Accomplishing these goals would deliver “world firsts” and produce record output power levels.

15. SUBJECT TERMS

16. SECURITY CLASSIFICATION OF:			17. LIMITATION OF ABSTRACT	18. NUMBER OF PAGES
a. REPORT	b. ABSTRACT	c. THIS PAGE		
U	U	U	SAR	43

19a. NAME OF RESPONSIBLE PERSON	19b. PHONE NUMBER *(Include area code)*
NATHANIEL LOCKWOOD	314-235-6005

Advanced Surface Artificial Materials for High Power Microwave Sources

Amy J. MacLachlan (Researcher)

Adrian W. Cross (Co-Investigator)

Alan D. R. Phelps (Principal Investigator)

University of Strathclyde, Glasgow, Scotland, UK

GRANT: FA9550-17-1-0095 P00004

Final Performance Report

Including SF298 Report Documentation Page

Period of Performance: 15 April 2017-14 April 2022

Final Version (Dated 31 May 2022)

TABLE OF CONTENTS

1. Abstract

Research results are reported of advanced cylindrical surface two-dimensional periodic surface lattice (2D PSL) structures for applications in high power microwave sources. 2D PSL structures enable highly overmoded sources to emit coherently at higher powers than conventional sources. The principle is independent of frequency from a few GHz up to THz frequencies. This research has produced several publications.

Analytical theory, combined with numerical modeling, has revealed several very promising new research routes. Recent results have highlighted the potential for higher performance 2D PSL sources using electron beams produced by advanced carbon nanotube cathodes. Exciting new research opportunities include phase locking of multiple 2D PSL oscillators, achieving superradiant 2D PSL sources and exploring the potential for powerful 2D PSL amplifiers. Accomplishing these goals would deliver “world firsts” and produce record output power levels.

2. Introduction

Conventional microwave radiation sources have interaction regions scaled to the source's intended operating wavelength λ_{op}, limiting the output power at high frequencies. Overcoming this challenge by increasing the cavity dimensions leads to multi-mode operation, detrimental to the efficiency of the device. Here, an innovative mode-coupling technique, involving the coupling of volume and surface fields in large cavities based on 'effective metadielectric' Periodic Surface Lattice (PSL) structures (or high-impedance surfaces) is proposed. The effect of the Covid pandemic during 2020-22 delayed the laboratory proof-of-principle experiments. During that period the research project progressed by concentrating effort on a series of numerical simulations that were run via remote access to computers on campus. Numerical simulations of the novel mode-selection method, using CST Microwave Studio (MWS) software, have demonstrated the effectiveness of this method of producing higher power outputs than the powers obtainable from conventional HPM sources. The results produced during this research project have been reported in a series of publications [1-18].

3. Analytical Theory

This analytical theory has been reported in publications [5-7,12] during this project and is summarized here to provide the fundamental physical principles that underpin the application of periodic surface lattices (PSLs) in overmoded high power microwave sources. This theory is applicable to both cylindrical PSLs and planar PSLs, based on the assumption that the mean radius of the cylinder r_0 is large in comparison to the operating wavelength ($r_0 \gg \lambda$), which has been made throughout this analysis. The PSL's eigenfield for the case of an oversized cylindrical PSL can be described as a superposition of a well-defined $TM_{0,T}$ volume field and high order $TM_{\bar{m},n}$ surface fields. Lattice synchronization is obtained by launching a near cut-off, symmetric $TM_{0,T}$ volume mode (where T and 0 are the number of radial and azimuthal variations respectively) through the structure, or in the case of planar geometry, by exciting a Fabry-Perot standing plane wave. The cylindrical PSL can be substituted for a smooth waveguide with a fictitious magnetic surface current density $\boldsymbol{j}_m$ (symbols in bold font indicate 3-vectors) in place of the corrugation to describe field coupling or scattering. Assuming r_0 is large, the theory developed for a cylindrical PSL is also relevant to the study of an equivalent planar PSL.

From Maxwell's curl equations, $\nabla^2 \boldsymbol{H} = -\omega^2 \varepsilon \mu \, \boldsymbol{H} + i\omega\varepsilon \boldsymbol{j}_m$ where $\varepsilon = \varepsilon_r \varepsilon_0$ and $\mu = \mu_r \mu_0$ denote respectively the permittivity and permeability in the 'effective metadielectric' material. In the theoretical study we take $\varepsilon_r = 1$ and $\mu_r = 1$ in the case of vacuum. When $r_0 \gg \lambda_{op}$ and providing the corrugation Δr is suitably shallow $(\Delta r \ll \lambda_{op})$ the PSL's eigenfield can be described as a superposition of waveguide modes (where the volume and surface modes have real and imaginary transverse wavenumbers respectively). The transverse electric ***E*** and magnetic ***H*** fields are expanded as a sum of the waveguide

modes $\boldsymbol{H}, \boldsymbol{E} = \sum_q (C_q(z), D_q(z))(\boldsymbol{H}_q, \boldsymbol{E}_q)$, allowing the field inside the finite cylinder to be described as a slow wave envelope filled with fast varying terms. The field inside the structure is decomposed as a set of eigenfields, where $C_q(z)$ and $D_q(z)$ are the slowly varying magnetic and electric eigenfield amplitudes respectively

$$\sum_q \nabla^2 (C_q(z)\boldsymbol{H_q}) = -\omega^2 \varepsilon\mu \sum_q C_q(z)\boldsymbol{H}_q + i\omega\varepsilon \boldsymbol{j}_m \quad (1a)$$

$$\sum_q \nabla^2 (D_q(z)\boldsymbol{E}_q) = -\omega^2 \varepsilon\mu \sum_q D_q(z)\boldsymbol{E}_q \quad (1b)$$

Eqs. (1a) and (1b) describe the structure's fields in their general form and volume and surface field amplitudes are introduced later in the theory. To describe succinctly the field distribution inside it is sufficient to define only the magnetic fields as the electric fields can be derived from them. The total power transmitted through the structure is defined by integrating the Poynting vector $\frac{1}{2}(\boldsymbol{E} \times \boldsymbol{H}^*)$ over the cylindrical cross section. This treatment is restricted to consider only the near cut-off volume mode ($\omega \approx \omega_0^v$) for which $k_z \to 0$ and $\lambda_z \to \infty$. In the case of a planar system, the structure is assumed to be infinitely large and edge effects are neglected. In practice, however, some detuning from the ideal situation where $\omega = \omega_0$ exists due to the structure's finite length. $\boldsymbol{E}\times \boldsymbol{H}^*$ is implicitly defined by multiplying both sides of Eq.(1a) by the complex conjugate of the transverse magnetic cut-off mode ($\boldsymbol{H}_{q'}^*$). Separating ∇^2 into its transverse and longitudinal components and substituting the Helmholtz equation $\nabla_\perp^2 \boldsymbol{H}_q + \frac{(\omega_0^q)^2}{c^2}\boldsymbol{H}_q = 0$ for the localized volume and surface fields into $\boldsymbol{H}_{q'}^* \cdot \sum_q \nabla_z^2 C_q(z)\boldsymbol{H}_q + \boldsymbol{H}_{q'}^* \cdot \sum_q \nabla_\perp^2 C_q(z)\boldsymbol{H}_q + \left(\frac{\omega}{c}\right)^2 \boldsymbol{H}_{q'}^* \cdot \sum_q C_q(z)\boldsymbol{H}_q = i\omega\varepsilon \boldsymbol{j}_m \cdot \boldsymbol{H}_{q'}^*$ gives

$$\boldsymbol{H}_{q'}^{*} \cdot \sum_q \nabla_z^2 C_q(z) \boldsymbol{H}_q + \boldsymbol{H}_{q'}^{*} \cdot \sum_q C_q(z) \left(\frac{\omega^2 - \omega_0^{\,2}}{c^2} \right) \boldsymbol{H}_q = i\omega\varepsilon \boldsymbol{j}_m \cdot \boldsymbol{H}_{q'}^{*} \tag{2}$$

where q' denotes the near-cut off volume mode. Imposing the orthogonality condition $\int_{S_\perp} \boldsymbol{H}_q \cdot \boldsymbol{H}_{q'}^{*}\, d\sigma = 0$ if $q \neq q'$ and integrating over the waveguide's cylindrical cross-section $S_\perp$, where $d\sigma$ is the differential element of surface area, gives the normalized wave equation. Small diffractive and Ohmic losses are considered by introducing detuning parameters. Here, we introduce detuning between the variable frequency ω and the system eigenfrequencies ω_0 and $\omega_0^{v,s}$ (where ω_0 is the cut-off frequency if no corrugation is introduced i.e. pure volume wave as an ideal solution of Helmholtz equation while $\omega_0^{v,s}$ are eigenfrequencies of the volume and surface fields respectively if corrugations are introduced) is $\frac{(\omega^2 - \omega_0^2)}{c^2}$ while the detuning between volume and surface modes is $\Delta = \omega_0^v - \omega_0^s \cong ck_z^v$. We note that as corrugations are shallow $\omega_0 \cong \omega_0^v$ while satisfying the Bragg resonance condition $\bar{k}_z = k_z^s - k_z^v$ for the near cut-off $(k_z^v \cong 0)$ $TM_{0,T}$ mode, requires that $\omega_B = \omega_0^s$. We define the Bragg detuning $\hat{\delta} = \frac{2(\omega_B - \bar{\omega}_0)}{c^2}$ in terms of the mean angular frequency, $\bar{\omega}_0 = \frac{\omega_0^v + \omega_0^s}{2}$ and incorporate $\hat{\delta}$ into the normalized wave equation. We note that $\hat{\delta}$ can be complex and its imaginary part describes the losses.

$$\nabla_z^2 C_q^{v,s}(z) + \omega\hat{\delta} C_q^{v,s}(z) \mp \frac{\bar{\omega}_0 \Delta}{c^2} C_q^{v,s}(z) = N_{v,s} \oint \boldsymbol{j}_m \cdot \boldsymbol{H}_{q'}^{*}\, d\sigma \tag{3}$$

$N_{v,s} = \frac{i\omega\varepsilon}{\oint_{S_\perp} \boldsymbol{H}_q \cdot \boldsymbol{H}_{q'}^{*} d\sigma}$ is the wave norm for the volume (v) and surface (s) modes, for which the "−" and "+" signs apply respectively. The integral $\oint_{S_\perp} \boldsymbol{H}_q \cdot \boldsymbol{H}_{q'}^{*}\, d\sigma$ denotes a closed surface integration with the boundaries defined by the smooth boundaries of the unperturbed waveguide.

Due to the structure's periodicity, it is possible to express the slowly varying surface field as a complex Fourier series of the form $C_q^s(z) = \sum_{n_s=-\infty}^{\infty} B_{n_s}(z) e^{in_s \bar{k}_z z}$ where B_{n_s} is the amplitude of the surface field's n_s harmonic. Likewise, the volume field can be written as a complex Fourier expansion using the approximation $k_{z,v} \cong \bar{k}_z = 2\pi/d_z$ which equates the volume field's longitudinal wavenumber to that of the structure and corresponds to the case of coherent, coupled eigenmode formation i.e. minimal detuning. Evaluating the second order partial differential terms and substituting into Eq. (3) yields wave equations for the volume Eq. (4a) and surface Eq. (4b) modes.

$$\sum_{n_v}\left(e^{in_v\bar{k}_z z}\frac{\partial^2 A_{n_v}(z)}{\partial z^2} + 2in_v\bar{k}_z e^{in_v\bar{k}_z z}\frac{\partial A_{n_v}(z)}{\partial z} - {n_v}^2{\bar{k}_z}^2 A_{n_v}(z)e^{in_v\bar{k}_z z}\right) +$$

$$\omega\hat{\delta}\left(\sum_{n_v} A_{n_v}(z)\, e^{in_v\bar{k}_z z}\right) - \frac{\bar{\omega}_0\Delta}{c^2}\left(\sum_{n_v} A_{n_v}(z)e^{in_v\bar{k}_z z}\right) = N_v \oint \boldsymbol{j}_m \cdot \boldsymbol{H}_q^*, d\sigma \qquad (4a)$$

$$\sum_{n_s}\left(e^{in_s\bar{k}_z z}\frac{\partial^2 B_{n_s}(z)}{\partial z^2} + 2in_s\bar{k}_z e^{in_s\bar{k}_z z}\frac{\partial B_{n_s}(z)}{\partial z} - n_s^2{\bar{k}_z}^2 B_{n_s}(z)e^{in_s\bar{k}_z z} +\right) +$$

$$\omega\hat{\delta}\left(\sum_{n_s} B_{n_s}(z)\, e^{in_s\bar{k}_z z}\right) - \frac{\bar{\omega}_0\Delta}{c^2}\left(\sum_{n_s} B_{n_s}(z)e^{in_s\bar{k}_z z}\right) = N_s \oint \boldsymbol{j}_m \cdot \boldsymbol{H}_q^*, d\sigma \qquad (4b)$$

where A_{n_v} is the amplitude of the n_v harmonic of the volume field. To evaluate the right-hand side of Eq. (4a, b) we must define $\boldsymbol{j}_m \cdot \boldsymbol{H}_q^*$. A cylindrical PSL with sinusoidal corrugation $l = r_0 + \Delta r cos(\bar{m}\varphi)\cos(\bar{k}_z z)$ and $\bar{m}$ azimuthal variations is equivalent to a smooth cylindrical waveguide when the magnetic surface current boundary condition $\boldsymbol{j}_m = \boldsymbol{n} \times \left(\boldsymbol{\nabla}(l\boldsymbol{E} \cdot \boldsymbol{n})\right) + i\omega l\boldsymbol{n} \times [\boldsymbol{n} \times \boldsymbol{H}]$ is satisfied. For planar geometry, $\bar{m}\varphi$ is substituted with $\bar{k}_y y$ where $\bar{k}_y = 2\pi/d_y$. Enforcing this condition gives $\boldsymbol{j}_m \cdot \boldsymbol{H}_q^* = i\omega l(z,\varphi)\left(\boldsymbol{E}_{q,n} \cdot \boldsymbol{E}_{q,n}^* + \boldsymbol{H}_{q,\tau} \cdot \boldsymbol{H}_{q,\tau}^*\right)$ where $\boldsymbol{E}_{q,n}$ and $\boldsymbol{H}_{q,\tau}$ are the normal electric and tangential magnetic field components with complex conjugates $\boldsymbol{E}_{q,n}^*$ and $\boldsymbol{H}_{q,\tau}^*$. In the case of a $TM_{0,T}$ volume mode (with no normal electric field component) $\boldsymbol{E}_{q,n} = 0$. Separating $\boldsymbol{H}_{q,\tau}$ into its volume

and surface field constituents $\boldsymbol{H}_{q,\tau} = \boldsymbol{H}^{v}_{q,\tau}(r)C^{v}_{q}(z) + \boldsymbol{H}^{s}_{q,\tau}(r,\varphi)C^{s}_{q}(z)$ and expanding to include the full set of eigenmodes gives

$$\boldsymbol{j}_m \cdot \boldsymbol{H}^{*}_{q} = i\omega\left[r_0 + \frac{\Delta r}{4}\left(e^{i\bar{m}\varphi} + e^{-i\bar{m}\varphi}\right)\left(e^{i\bar{k}_z z} + e^{-i\bar{k}_z z}\right)\right]\boldsymbol{H}^{*,v}_{q,\tau} \cdot \left(\boldsymbol{H}^{v}_{q,\tau}(r)\sum\nolimits_2 C^{v}_{q}(z) + \boldsymbol{H}^{s}_{q,\tau}(r)\cos(m_s\varphi)\sum\nolimits_{n_s} B_{n_s}(z)e^{in_s\bar{k}_z z}\right) \quad (5)$$

The $\boldsymbol{j}_m \cdot \boldsymbol{H}^{*}_{q}$ term is now integrated over the cylindrical cross section $d\sigma$, where $N'_{v,s}\oint \boldsymbol{j}_m \cdot \boldsymbol{H}^{*(v,s)}_{q,\tau}\, d\sigma = N'_{v,s}\int_0^{2\pi} r\left(\boldsymbol{j}_m \cdot \boldsymbol{H}^{*}_{q}\right)\big|_{r=r_0} d\varphi$ and $N'_{v,s} = i\omega N_{v,s}$. One of the necessary criteria for volume and surface mode coupling is $\oint \boldsymbol{j}_m \cdot \boldsymbol{H}^{*}_{q}\, d\sigma \neq 0$. This requirement is satisfied by averaging over the period of fast oscillations from 0 to 2π, neglecting exponential (oscillating) terms that would otherwise integrate to zero. The fundamental volume field harmonic $(n_v = 0)$ is first described in the form $\oint \boldsymbol{j}_m \cdot \boldsymbol{H}^{*}_{q}\, d\sigma = r_0^2 N'_v \int_0^{2\pi}(I)|_{r=r_0}\, d\varphi$ where *I* is the integrand, composed of four terms

(1) $\boldsymbol{H}^{*v}_{q,\tau}(r) \cdot \boldsymbol{H}^{v}_{q,\tau}(r)\sum\nolimits_2 C^{v}_{q}(z)$

(2) $\boldsymbol{H}^{*v}_{q,\tau} \cdot \boldsymbol{H}^{s}_{q,\tau}(r)\cos(m_s\varphi)\sum\nolimits_{n_s} B_{n_s}(z)e^{in_s\bar{k}_z z}$

(3) $\frac{\Delta r}{4r_0}\left(e^{i\bar{m}\varphi} + e^{-i\bar{m}\varphi}\right)\left(e^{i\bar{k}_z z} + e^{-i\bar{k}_z z}\right)\boldsymbol{H}^{*v}_{q,\tau} \cdot \boldsymbol{H}^{v}_{q,\tau}(r)\sum\nolimits_2 C^{v}_{q}(z)$

(4) $\frac{\Delta r}{4r_0}\left(e^{i\bar{m}\varphi} + e^{-i\bar{m}\varphi}\right)\left(e^{i\bar{k}_z z} + e^{-i\bar{k}_z z}\right)\boldsymbol{H}^{*v}_{q,\tau} \cdot \boldsymbol{H}^{s}_{q,\tau}(r)\cos(m_s\varphi)\sum\nolimits_{n_s} B_{n_s}(z)e^{in_s\bar{k}_z z}$

Terms 2 and 4 demonstrate scattering and potential coupling of volume and surface fields. The geometric parameter $\frac{\Delta r}{r_0}$ is closely linked to the coupling coefficient. Discarding terms 2 and 3 (which integrate to zero after averaging over the fast oscillation terms) and employing the trigonometric identity $cos(m_s\varphi) = 1/2\left(e^{im_s\varphi} + e^{-im_s\varphi}\right)$ gives

$$\oint \boldsymbol{j}_m \cdot \boldsymbol{H}_q^* \, d\sigma = r_0^2 N_v' \int_0^{2\pi} \Big(\boldsymbol{H}_{q,\tau}^{*v}(r_0) \cdot \boldsymbol{H}_{q,\tau}^{v}(r_0) \sum_2 C_q^v(z) + \frac{\Delta r}{8r_0} \boldsymbol{H}_{q,\tau}^{*v}(r_0) \cdot \boldsymbol{H}_{q,\tau}^{s}(r_0) \left(e^{i\bar{k}_z z} + e^{-i\bar{k}_z z} \right) \left(e^{i\bar{m}\varphi} + e^{-i\bar{m}\varphi} \right) \left(e^{im_s\varphi} + e^{-im_s\varphi} \right) \sum_{n_s} B_{n_s}(z) e^{in_s \bar{k}_z z} \Big) \Big|_{r=r_0} d\varphi \quad (6)$$

A non-trivial result is obtained only when $m_s = \bar{m}$, forcing the fast oscillation terms to vanish. Based on the azimuthal Bragg condition, $\bar{m} = m_v + m_s$, we establish that $m_v = 0$, justifying the role of the azimuthally symmetric $TM_{0,T}$ volume mode. The remaining fast oscillation terms are eliminated when $n_s = \pm 1$. Until now, only the fundamental harmonic of the volume field has been considered. For completeness, and to provide a more thorough mathematical description of the possible scattering processes, the Fourier expansion of both fields is included, allowing different low order values of n_v and n_s to be explored. We follow a similar procedure to that above, now multiplying $\boldsymbol{j}_m \cdot \boldsymbol{H}_q^*$ by $e^{-i\bar{k}_z z n_{v,s}}$ to describe possible coupling mechanisms involving the $n_{v,s} = 0$ and $n_{v,s} = \pm 1,2$ field harmonics. The scattering of the $n_v = 0$ volume field into the surface field is described by the expression

$$\pi {r_0}^2 N_v' \left(\boldsymbol{H}_{q,\tau}^{*,v}(r_0) \cdot \boldsymbol{H}_{q,\tau}^{v}(r_0) \sum_{n_v} A_{n_v}(z) + \frac{\Delta r}{2r_0} \boldsymbol{H}_{q,\tau}^{*,v}(r_0) \cdot \boldsymbol{H}_{q,\tau}^{s}(r_0) \sum_{n_s} B_{n_s}(z) \left(e^{i\bar{k}_z z(1-n_v+n_s)} + e^{i\bar{k}_z z(-1-n_v+n_s)} \right) \right) \quad (7)$$

For a non-zero result after integrating, the conditions $1 - n_v + n_s = 0$; $n_s^1 = n_v - 1$ and $-1 - n_v + n_s = 0$; $n_s^2 = n_v + 1$ must hold true demonstrating the potential for coupling of the fundamental volume field and $n_s \pm 1$ surface field harmonics. Likewise, scattering between the $n_v \pm 1$ and $n_s = 0, \pm 2$ harmonics is also possible. Scattering of the surface field into the volume field is investigated in a similar manner, multiplying Eq.(5) by $e^{-i\bar{k}_z z n_s}$.

Expanding and neglecting the same terms as before gives the following expression after integration:

$$\pi {r_0}^2 N_s' \left(\boldsymbol{H}_{q,\tau}^{*,s}(r_0) \cdot \boldsymbol{H}_{q,\tau}^{s}(r_0) \sum_{n_s} B_{n_s}(z) + \frac{\Delta r}{2r_0} \boldsymbol{H}_{q,\tau}^{*,s}(r_0) \cdot \boldsymbol{H}_{q,\tau}^{v}(r_0) \sum_{n_v} A_{n_v}(z) \left(e^{i\bar{k}_z z(1-n_s+n_v)} + e^{-i\bar{k}_z z(1+n_s-n_v)} \right) \right) \quad (8)$$

This expression is comprised of two parts, the first describing the accumulation of a localized surface field (which has a dissipative effect and does not contribute to the coupling of volume and surface fields) and the second defining scattering of the surface field into the volume field. Once again, to eliminate the exponential terms and obtain a non-zero result, the following conditions must be met: $1 - n_s + n_v = 0$; $n_v^1 = n_s - 1$ and $1 + n_s - n_v = 0$; $n_v^2 = n_s + 1$. Coupling coefficients are introduced to describe the mutual resonant scattering (i.e. the volume field coupling with the surface field α_{vs} and the surface field coupling with the volume field α_{sv}) leading to the following set of coupled wave equations.

$$\nabla_z^2 C_q^v(z) + \omega\hat{\delta} C_q^v(z) - \frac{\bar{\omega}_0 \Delta}{c^2} C_q^v(z) = N_v \oint \boldsymbol{j}_m \cdot \boldsymbol{H}_{q'}^* \, d\sigma \quad (9a)$$

$$\nabla_z^2 C_q^s(z) + \omega\hat{\delta} C_q^s(z) + \frac{\bar{\omega}_0 \Delta}{c^2} C_q^s(z) = N_s \oint \boldsymbol{j}_m \cdot \boldsymbol{H}_q^* \, d\sigma \quad (9b)$$

$$\frac{\partial^2 A_n(z)}{\partial z^2} + 2i(n)\bar{k}_z \frac{\partial A_n(z)}{\partial z} - {\bar{k}_z}^2 (n)^2 A_n(z) + \left(\omega\widehat{\delta} - \frac{\bar{\omega}_0 \Delta}{c^2} \right) A_n(z) = \alpha_{vs} \left(B_{n-1}(z) + B_{n+1}(z) \right) \quad (9c)$$

$$\frac{\partial^2 B_n(z)}{\partial z^2} + 2i(n)\bar{k}_z \frac{\partial B_n(z)}{\partial z} - {\bar{k}_z}^2 (n)^2 B_n(z) + \left(\omega\widehat{\delta} + \frac{\bar{\omega}_0 \Delta}{c^2} \right) B_n(z) = \alpha_{sv} \left(A_{n-1}(z) + A_{n+1}(z) \right) \quad (9d)$$

Combining these coupling coefficients into a single parameter, we define $\alpha = \sqrt{\alpha_{vs}\alpha_{sv}}$. Finally, new amplitude constants, $\tilde{A}_{n_v}(z) = A_{n_v}(z)\sqrt{\alpha_{sv}}/\sqrt{\alpha_{vs}}$ and $\tilde{B}_{n_s}(z) =$

$B_{n_s}(z)\sqrt{\alpha_{vs}}/\sqrt{\alpha_{sv}}$ are introduced to give the following normalized coupled wave equations:

$$\frac{\partial^2\tilde{A}_n(z)}{\partial z^2}+2i(n)\bar{k}_z\frac{\partial\tilde{A}_n(z)}{\partial z}-\bar{k}_z{}^2(n)^2\tilde{A}_n(z)+\left(\omega\hat{\delta}-\frac{\bar{\omega}_0\Delta}{c^2}\right)\tilde{A}_n(z)=\alpha\big(B_{n-1}(z)+B_{n+1}(z)\big) \quad (10a)$$

$$\frac{\partial^2\tilde{B}_n(z)}{\partial z^2}+2i(n)\bar{k}_z\frac{\partial\tilde{B}_n(z)}{\partial z}-\bar{k}_z{}^2(n)^2\tilde{B}_n(z)+\left(\omega\hat{\delta}+\frac{\bar{\omega}_0\Delta}{c^2}\right)\tilde{B}_n(z)=\alpha\big(A_{n-1}(z)+A_{n+1}(z)\big) \quad (10b)$$

where the normalized coupling coefficient α is defined as

$$\alpha=\frac{\pi r_0\Delta r}{2}\sqrt{N_v'N_s'\big(\boldsymbol{H}_{q,\tau}^{*,v}(r_0)\cdot\boldsymbol{H}_{q,\tau}^{s}(r_0)\big)\left(\boldsymbol{H}_{q,\tau}^{*,s}(r_0)\cdot\boldsymbol{H}_{q,\tau}^{v}(r_0)\right)} \quad (11)$$

A coupled dispersion equation incorporating α and describing the structure's coupled eigenfield is derived

$$(\omega_e^2-\Lambda^2)[\Lambda^4-2\Lambda^2(2+\Gamma^2+\omega_e^2)+(2-\Gamma^2+\omega_e^2)^2]=2\alpha^4(2-\Gamma^2+\omega_e^2-\Lambda^2) \quad (12)$$

where Λ is the normalised wave vector, $\omega_e=\sqrt{\delta^2+2\delta+\widetilde{\Delta}^2}$ is a variable angular frequency and $\delta=(\omega-\Omega)/\Omega$, $\widetilde{\Delta}=\Phi/\Omega$, $\Gamma=2\bar{k}_zc/((\omega_0^v)^2+(\omega_0^s)^2)$ are renormalized detuning parameters with constants $\Phi,\Omega=\sqrt{((\omega_0^s)^2\mp(\omega_0^v)^2)/2}$. Solving Eq. (12) involves performing an integral mode calculation around the cylindrical surface.

4. Numerical simulations

The theory is applicable over a broad frequency range from infrared to terahertz and the output frequency is determined by the precise lattice parameters and geometry. Over the course of this project, simulations have been carried out at a series of frequencies including 35 GHz, 75 GHz, 94 GHz, 140 GHz, 200 GHz, 350 GHz and 395 GHz to demonstrate the scalability of the 2D PSL structures. Cylindrical 2D PSLs with a

cosinusoidal corrugation have been modeled using the Particle-in-Cell (PIC) solver of CST Microwave Studio. The corrugation on the inner wall of the 2D PSL is defined:

$$r = r_0 + \Delta r cos(k_z z) cos(\bar{m}\varphi) \quad (13)$$

where r_0 is the mean radius, Δr is the amplitude of the azimuthal and axial corrugation, and $\bar{m}$ is the number of azimuthal variations around the cylindrical cross section. The azimuthal period $d_m = 2\pi r_0/\bar{m}$ is constrained by the wave-beam coupling criterion $\bar{m} \leq 2\pi r_0/\lambda\gamma$ where γ is the relativistic factor and λ is the wavelength. To enable the intended wave-beam interaction, the axial period $d_z = 2\pi/k_z$ of the structure is shortened to match the axial electron beam velocity, $v_z = c\left(1 - (1/\gamma)^2\right)^{1/2}$.

A diagrammatic representation of the 2D PSL CST MWS model is presented in Fig.1. Dissipative wall losses are considered by simulating the metallic wall of the 2D PSL as a lossy, annealed copper surface with conductivity, σ =5.8e+07 S/m. Reflection at z_a and z_b (where the PSL begins and ends) is mitigated by the inclusion of 2 tapered corrugation lengths. The length of each taper is equal to one axial period, d_z, giving the PSL a total length, $L=(n+2)d_z$. Sections of smooth cylindrical waveguide are positioned between (i) the input taper and the cathode and (ii) the output taper and the waveguide port as shown.

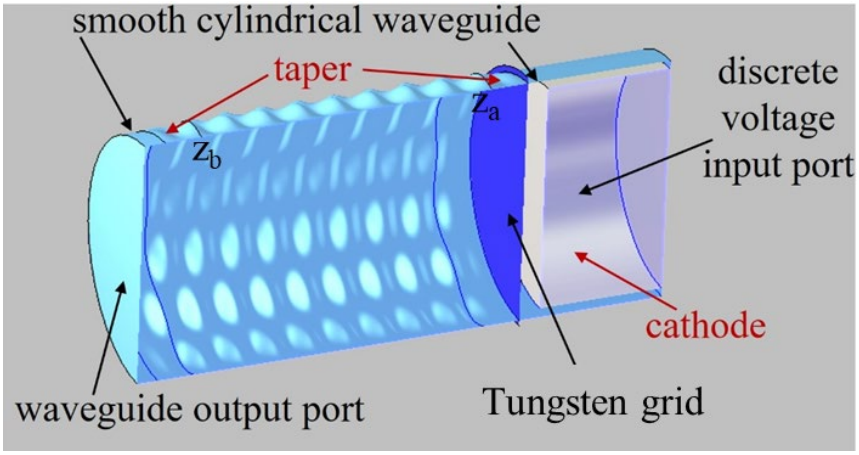

Fig.1 Diagram of CST Microwave Studio 2D PSL oscillator model

The electron beam must pass sufficiently close to the corrugated wall in order to intercept the exponentially decaying surface field that protrudes beyond the lattice corrugation. The transparent tungsten grid (with electrical conductivity σ =1.89e+07 S/m) positioned between the cathode and the 2D PSL taper, allows electrons to be injected close to the corrugated surface. The beam is narrow in radial extent, and launched from an annular emission site on a flat cathode. Electrons are accelerated directly towards the grid from the field immersed cathode with minimal perpendicular velocity $(v_\perp/v_\parallel \cong 0.01)$. This model can be reproduced in the laboratory by using an annular thermionic cathode or by embedding carbon nanotubes in an annular ring to create a novel carbon nanotube (CNT) cathode . The exploitation of CNT cathodes to enhance these novel 2D PSL sources provides an exciting future research opportunity.

Simulations have been carried out to investigate the impact of the velocity spread of the electron beam on the performance of the device. Introducing a 5% velocity spread at the cathode emitter had little impact on the output efficiency due to the electron velocities

entering the 2D-PSL being primarily conditioned by the grid voltage. To provide a more realistic test the model was adapted to impose a velocity spread on the electrons emanating from the tungsten grid. The efficiency and power do not decrease for a 5% velocity spread introduced at the grid. However, when the spread is increased to 10%, although the spectral purity remains good, the efficiency and power start to decline, and for a 20% spread, the device no longer performs as expected. These results demonstrate the importance of achieving and maintaining a high quality electron beam, especially when considering a practical, laboratory device.

For practical reasons, such as the availability of diagnostic and experimental equipment (including state-of the-art cryogen-free magnets that will eventually replace the liquid helium superconducting magnet in the W-band 2D PSL experiment described in section 5) it can be advantageous to initially design 2D PSL oscillators at high frequencies, with the option to later modify the structure's parameters for any chosen operating frequency.

350GHz Simulation Results

Theoretical and numerical studies and simulations have been carried out at 350GHz for a 2D PSL with a diameter to wavelength ratio of $D/\lambda = 3.5$. The parameters of the 2D PSL and electron beam are presented in Table 1. Fig.2 demonstrates the particle energy as a function of axial position for the 2D PSL and electron beam parameters given in Table 1. The electron beam becomes increasingly modulated with the wave-beam interaction reaching saturation after only 6ns. The high quality electron beam shown in Fig.2 is essential to the efficient operation of the device.

Quantity	Parameter Value	
Mean radius, r_0 (mm)	1.47	
Number of azimuthal variations, $\bar{m}$	10	
Corrugation amplitude, Δr (mm)	0.12	
Axial period, d_z (mm)	0.39	0.32
Electron beam voltage (kV)	85-89	52
Electron beam current (A)	90	

Table.1 350 GHz 2D PSL and electron beam parameters

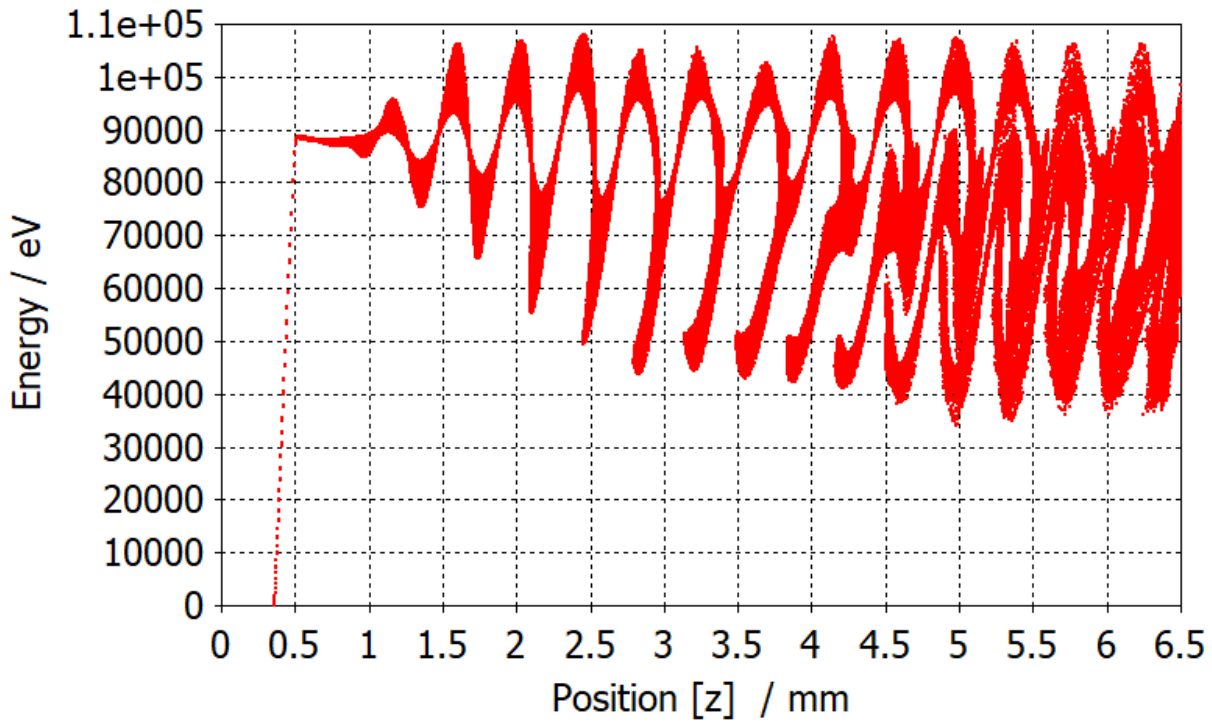

Fig.2 Electron energy (eV) of the 89kV, 90A thin, annular electron beam after 6ns

Fig. 3 compares the output spectra of an oscillator based on a 2D PSL (solid red plot) to an equivalent 1D PSL (dotted black plot). In both cases, the transporting magnetic field is 5T and the separation between the inner cavity wall and the 0.1mm thick annular beam is 0.055mm. The results justify the use of the more complex two-dimensional geometry by highlighting the significant improvements in power, spectral purity and output efficiency, observed in the 2D PSL simulations.

Fig.4 shows that even higher output power is obtained when the guiding magnetic field is reduced to 3T and the electron beam is positioned closer to the wall (0.033mm) where it can better intercept the surface field. Replicating this same set-up for the 1D case, resulted in electrons being lost to the wall. The results in Fig.4 are plotted on (1) a logarithmic scale (left) with around 6 orders of magnitude dynamic range and (2) a linear scale (right) to illustrate the narrow, high Q-cavity eigenmode. The successful operation of the device and single frequency output is attributed to the coupling of volume and surface fields in the overmoded 2D PSL interaction cavity. No parasitic gyrotron interactions are observed due to the suppression of the perpendicular beam velocity $v_{\perp}$.

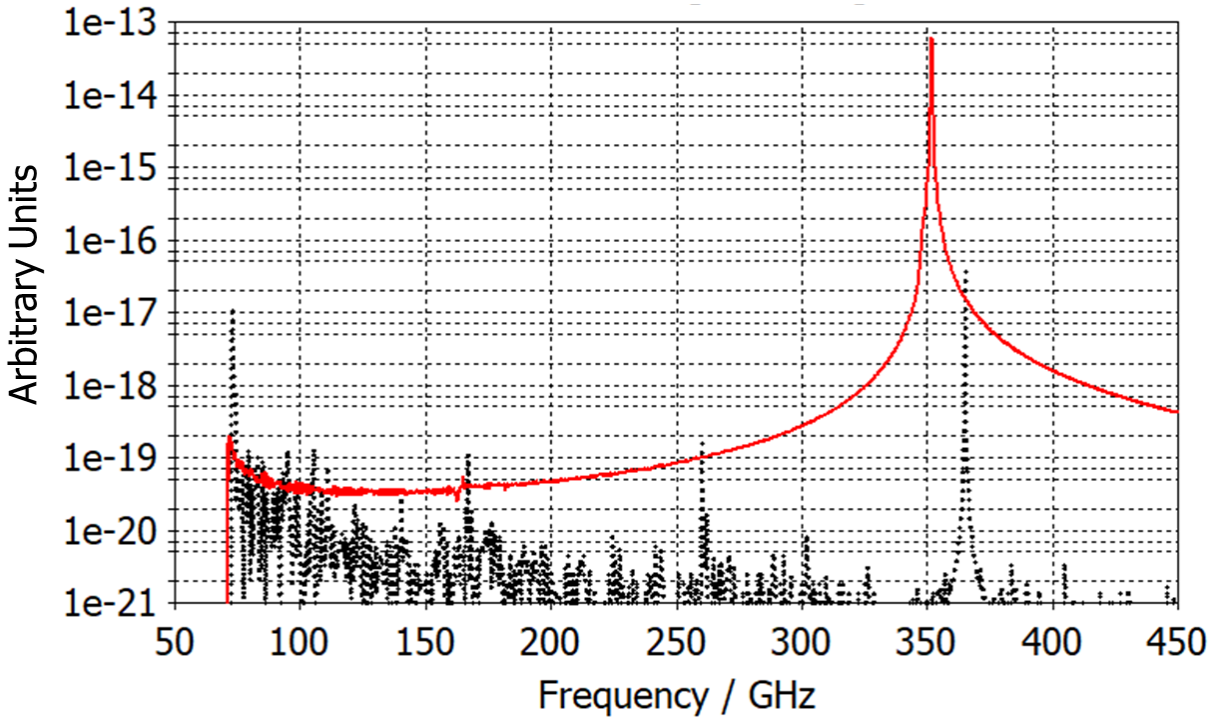

Fig.3 Electron energy (eV) of the 89kV, 90A thin, annular electron beam after 6ns

The harmonic content of the output (at around 700 GHz) has a reasonably low power level as demonstrated in Fig.5. Plots of the output power (left) and efficiency (right) as a function of time for the lossy, copper, 350GHz 2D PSL driven by the 89kV electron beam are presented in Fig.6. By employing advanced , high precision manufacturing techniques, the 1.95MW output power and 24% electronic efficiency should be reproducible in a laboratory experiment. However, transmission losses in the grid (which have not been considered in this model) are expected to reduce the efficiency by around 3%. A depressed collector can be incorporated into the 2D PSL oscillator to enable energy recovery and enhance the power level and efficiency of the device.

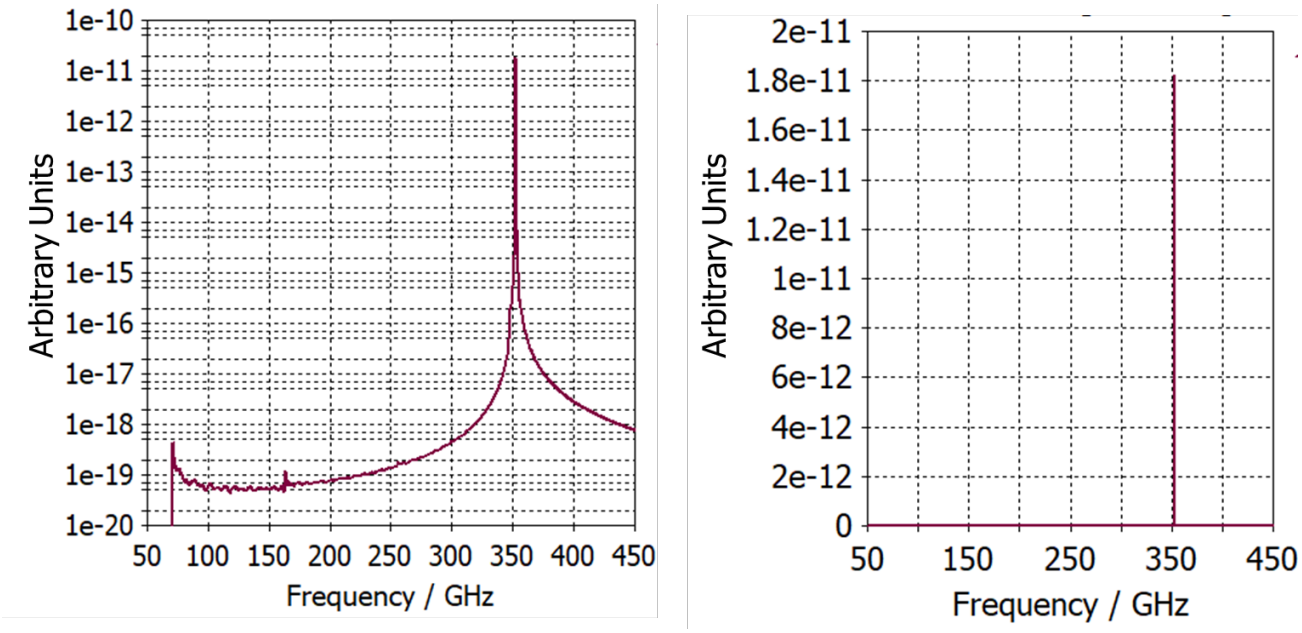

Fig.4 Output spectra of 350GHz 2D PSL and 89kV electron beam plotted on a log (left) and linear (right) scale

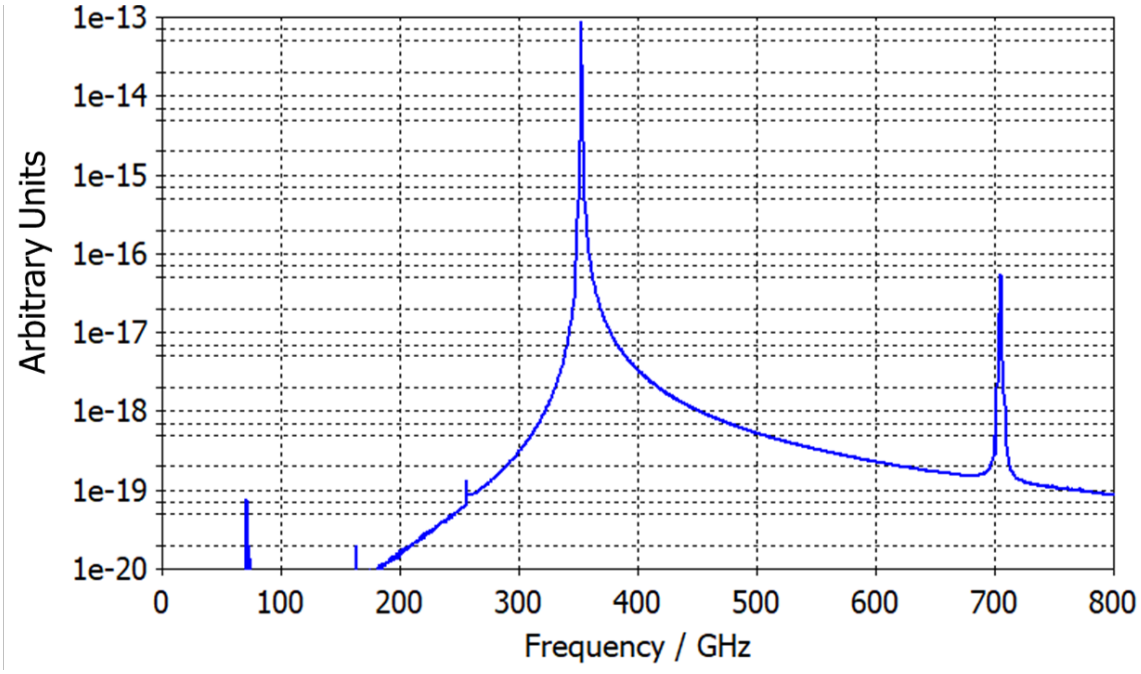

Fig.5 Output spectrum showing spatial harmonic around 700GHz for a 2D PSL designed to operate at 350GHz.

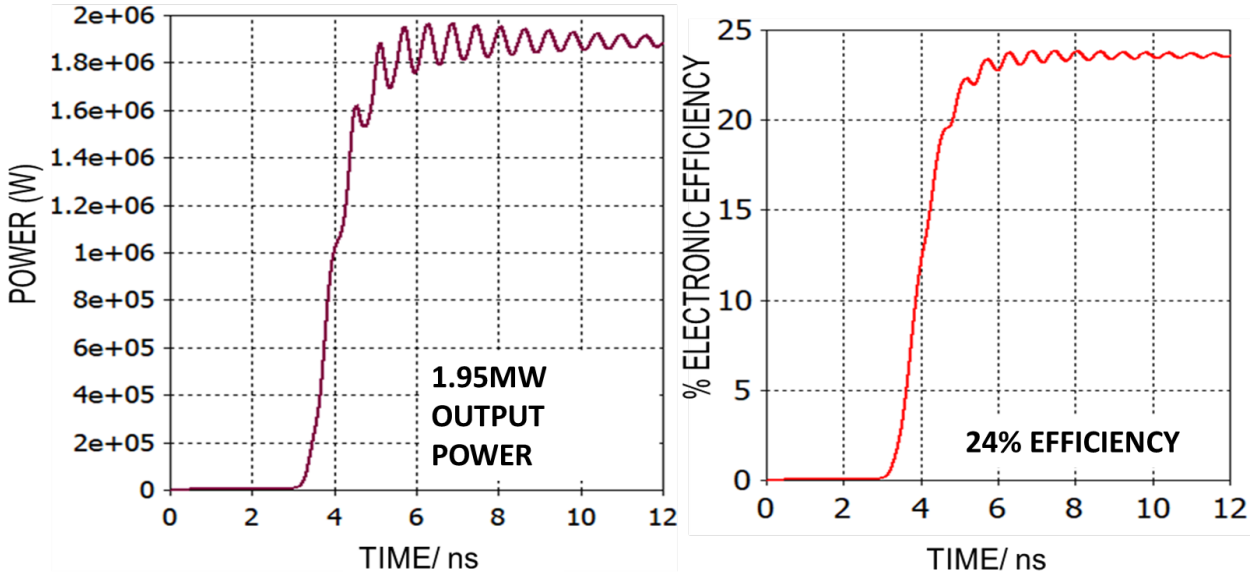

Fig. 6. Plots showing nearly 1.95MW of output power (left) and 24% efficiency (right) for the 2D PSL with d_z=0.39mm when simulated with a 3T B-field and a 0.033mm beam-wall separation.

The relatively modest 3T magnetic field is considerably lower than the magnetic field required for gyrotrons operating at the same frequency and is convenient for deployment in applications requiring compact, powerful, pulsed sources. Simulations show that this magnetic field can be reduced as low as 1.5T, albeit with a reduced electronic efficiency of around 10.5%. The electronic efficiency as a function of the magnetic field is plotted in Fig.7.

The output spectrum for a 2D PSL with a shorter, d_z=0.32mm axial period designed to be compatible with a lower voltage, 52kV electron beam is presented in Fig.8. The results show that the output frequency can be maintained when applying different electron beam voltages by appropriately scaling the lattice period, d_z. In this case a lower, 17% efficiency is observed. The theoretical and numerical studies suggest that different

operating regimes are possible depending on the parameters of the 2D PSL cavity and electron beam as well as the proximity of the beam to wall.

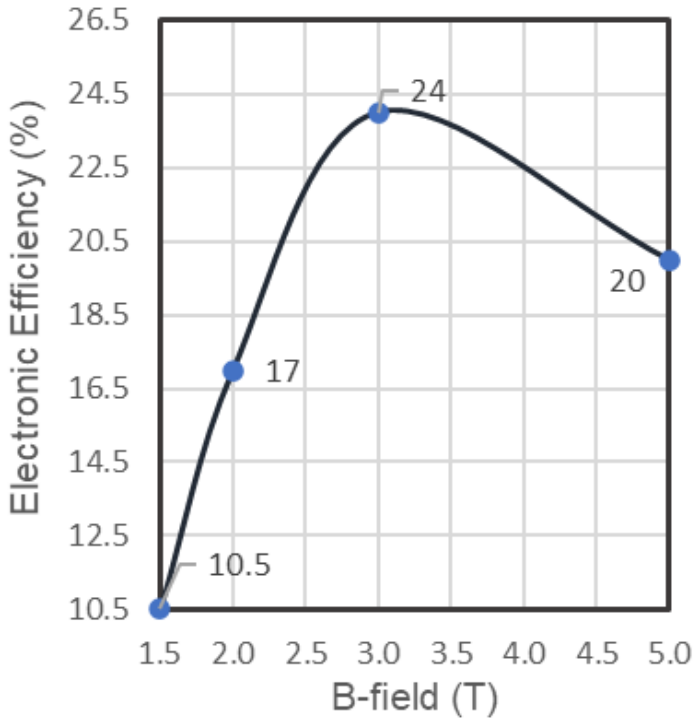

Fig.7 Electronic Efficiency as a function of magnetic field

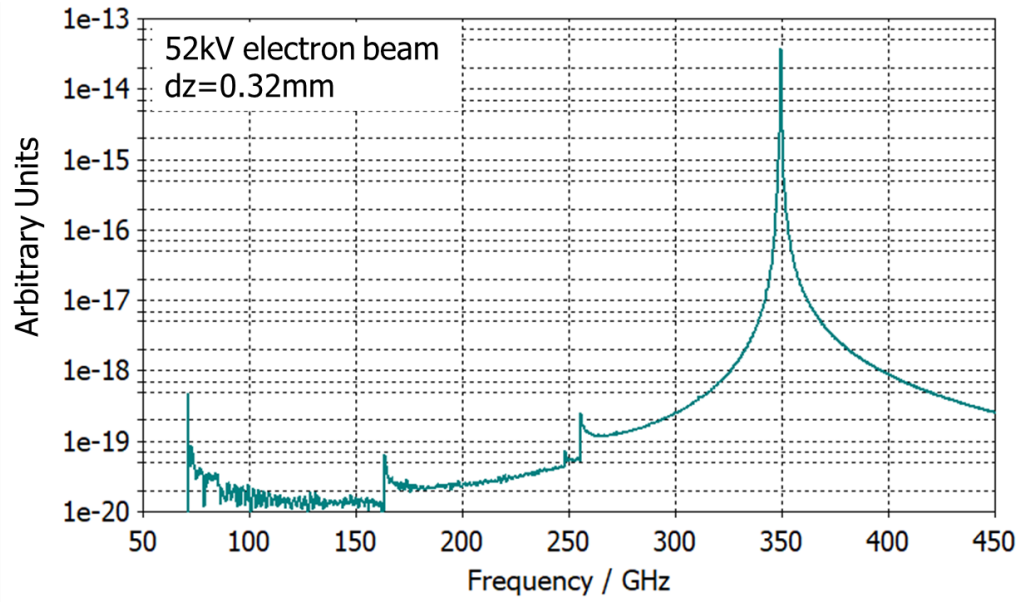

Fig. 8. Output spectrum of 350 GHz 2D PSL with d_z=0.32mm and 52kV electron beam.

Theoretical dispersion plots demonstrate how modifying the PSL and electron beam parameters can affect the operating regime, and consequently the efficiency, of the device. The dispersive properties of the 2D cavities are plotted by solving the coupled dispersion relation, Eq.(12). The modulated electron beam is described using the oscillating term, $\bar{k}_z v_z = \Omega_p$ which is relevant to all gyro or slow wave devices based on a periodic structure, particularly when the beam passes close to the corrugated wall. The electron beam that interacts with the synchronous, coupled cavity eigenmode of the 2D PSL is described:

$$\omega = k_z v_z + \frac{2\pi}{d_z} v_z \tag{14}$$

The coupled dispersion diagram presented in Fig.9 shows how changing the lattice period alters the shape of the dispersion, determining whether a backward wave, or a pi-mode or a forward wave interaction takes place. Fig.9 illustrates the coupled eigenfield dispersions for the (i) d_z=0.32mm PSL(grey curve) and (ii) the d_z=0.39mm PSL (red curve) which interact with the (i) 50kV (dot-dashed beam line) and (ii) 85kV (dashed beam line) and 89kV (solid beam line) electron beams. Simulations reveal that the voltage can be tuned within a few volts which, in certain cases, might change the operating regime.

Electrons interact with the lower dispersion branch in Fig.9 at 348- 349GHz. This branch has an especially slow group velocity, resulting in near stationary, localized interactions. Similar flattened dispersion curves have been observed in ‘mode-locked’ planar PSL structures (see refs 5-7,12).

In the top left inset, *1* depicts a near pi-mode interaction between the d_z=0.39mm 2D PSL and the 89kV beam (where $\bar{m} \sim 2\pi r_0/\lambda\gamma$). This corresponds to the set of results showing 1.95MW power and 24% efficiency in Figs.3-6. Point 2 (inset) marks a backward wave interaction between the same d_z=0.39mm 2D-PSL and a 85kV beam. Simulations based on these parameters showed an interaction around 350GHz with a lower 16% efficiency. The backward-wave interaction between the d_z=0.32mm, 2D-PSL and the 52kV beam, in *3* corresponds to the results in Fig.8.

Fig.10 shows the output power and efficiency of the 2D-PSL oscillator as a function of current. Simulations show that the device performs well with currents as low as 20A. The ability to reduce the current whilst still maintaining reasonably powerful radiation at the intended 350GHz frequency demonstrates the potential to develop larger diameter pulsed or continuous sources. The lower current cases (red dashed lines) are operating in a slightly different regime to the higher current cases (solid black lines) that correspond to the results shown in Figs. 3-6. Simulations show a lower effective beam energy at smaller currents which therefore shifts the operating point on the dispersion curves. Consequently, a backward wave interaction can become to a π-mode interaction , or vice versa, depending on the lattice parameters.

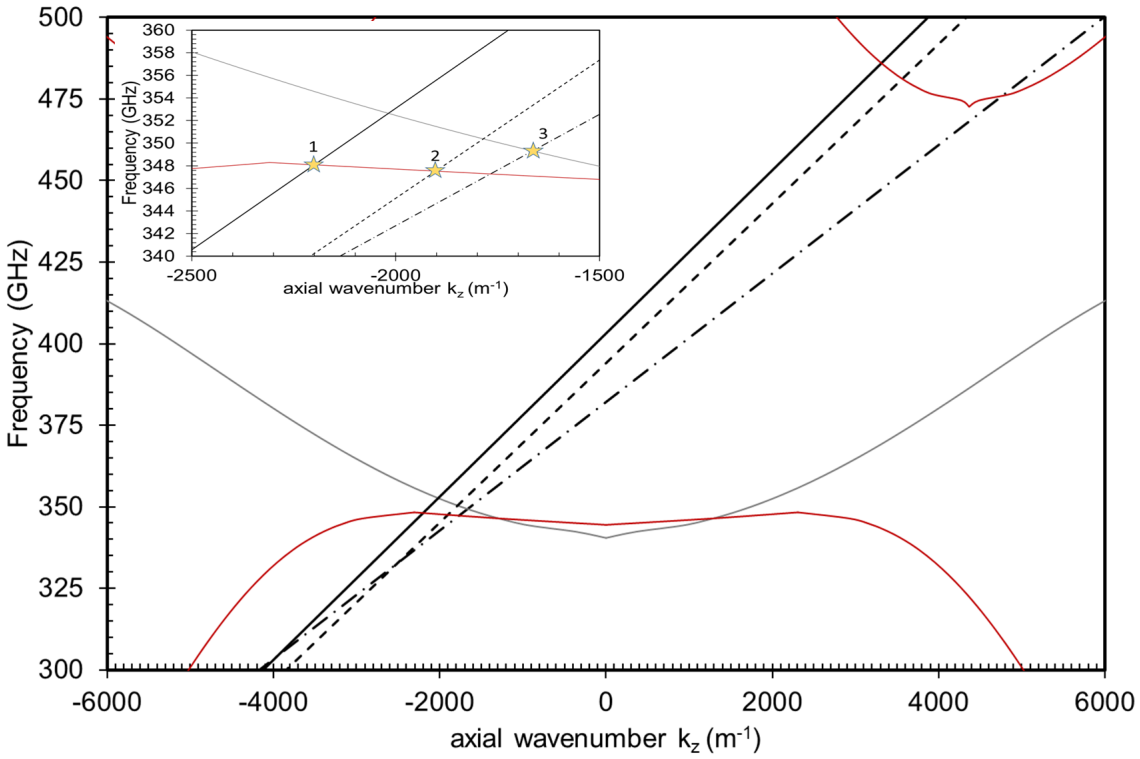

Fig. 9. Dispersion diagrams for the 2D PSL with axial period, 0.32mm (grey plot) and 0.39mm (red plot) showing possible interactions with 50kV (dot-dashed), 85kV (dashed) and 89kV(solid) electron beams. The top left-hand inset shows the 3 points of interaction and demonstrates the potential for an interaction close to the pi-point (1) as well as backward wave interactions (2,3). The slow group velocity observed at (1) and (3) facilitates the volume and surface mode coupling.

It is possible that the higher current regime is above a certain threshold current which must be exceeded in order to excite a particular regime of operation. A similar trend is observed in the increase of the rate of growth (shown via the decrease in time to reach the maximum output) as the current increases, for the lower and higher current regimes.

No direct correlation between efficiency and voltage is observed. The operating frequency is maintained for different voltages by adjusting d_z accordingly and, while altering the voltage changes the point at which the electron beam intersects the dispersion curve, this shift is counteracted by the corresponding change in d_z which

controls the modulated electron beam parameter, $\Omega_p = 2\pi d_z / v_z$. Simulations have shown successful operation of the device with lower voltages of around 30kV.

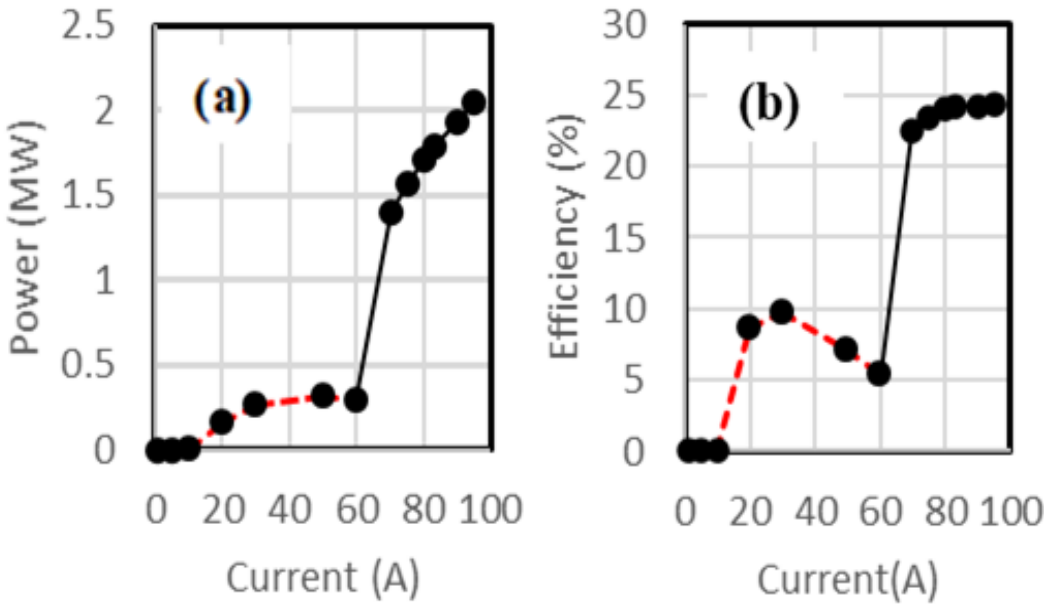

Fig. 10. Plots of beam current vs (a) output power and (b) efficiency showing two distinct regimes of operation distinguished by the dashed red and solid black lines.

The contour plots presented in Fig.11 show the axial electric field E_z evolution of the HE10,1 coupled cavity eigenmode at various locations throughout the structure including (a) the waveguide output; (b) the cylindrical waveguide section between the PSL and the output; (c) the center of the 2D PSL and (d) near the start of the 2D PSL. The contour plots in (b) to (c) show a clear superposition of the partial volume and surface fields that constitute the hybrid cavity eigenmode. The surface field is dominant in (d) but at the cylindrical waveguide output (a), the axial electric field clearly resembles a propagating $TM_{0,4}$ volume mode. This 'partial' volume mode output reduces the need for a complex mode converter, when compared to cases where the output radiation is strongly bound

to the cavity wall.

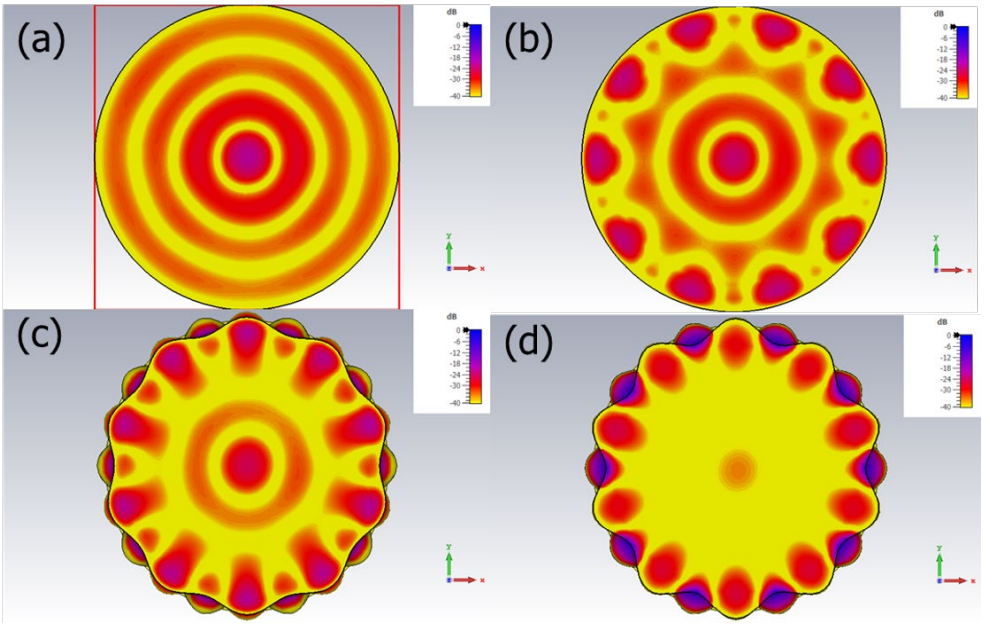

Fig. 11. Contour plots showing the partial volume and surface field components of the E_z $HE_{10,1}$ cavity eigenfield at the (a) output, (b) cylindrical waveguide, (c) center of 2D PSL and (d) near the start of the 2D PSL.

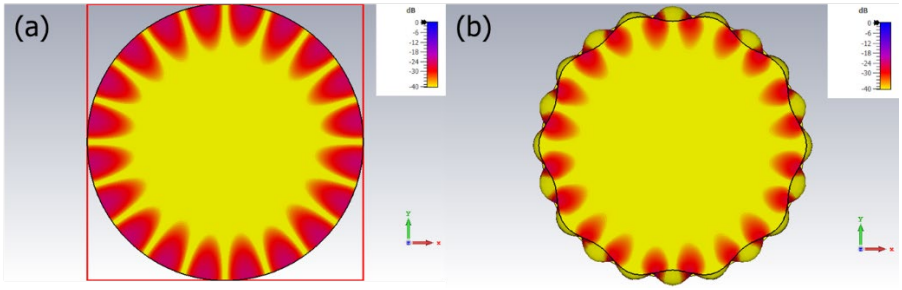

Fig. 12. Contour plots showing the axial magnetic field at (a) the waveguide output and (b) in the center of the 2D PSL, confirming the hybrid nature of the $HE_{10,1}$ cavity eigenfield.

Fig.12 shows the axial magnetic field H_z at (a) the cylindrical waveguide output and (b) in the center of the 2D PSL, demonstrating the hybrid character of the coupled cavity eigenmode. In accordance with the theory, the azimuthally symmetric volume field, $m_v = 0$ and the surface field with azimuthal index, $m_s = 10$ satisfy the azimuthal Bragg resonance condition, $\bar{m} = m_s + m_v$.

The tangential contour plots at the (a) waveguide output and (b) in the center of the 2D PSL presented in Fig.13 show the tangential partial volume and surface fields, involved in the mutual resonant volume and surface field scattering and resultant coupled eigenmode formation.

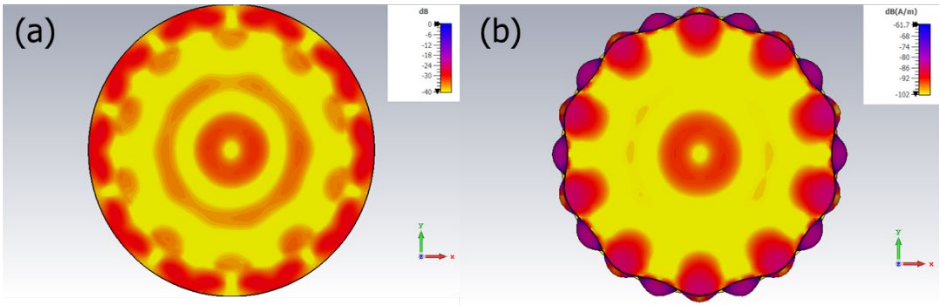

Fig. 13. Contour plots showing the partial volume and surface field components of the tangential magnetic field component of the $HE_{10,1}$ cavity eigenfield at the (a) waveguide output and (b) center of the 2D PSL.

75 GHz Simulation Results

Preliminary simulations have been carried out at 75 GHz for a 2D PSL with a mean radius of 10mm (D/λ=5) with a corrugation amplitude of 0.6mm and axial period, d_z=1.50mm designed to be compatible with a 55kV electron beam. The contour plots in Fig.14 show the axial electric (left) and tangential magnetic (right) field components in the center of the 2D PSL. The partial $TM_{0,6}$ volume and $HE_{16,1}$ surface field components are clearly visible, demonstrating the hybrid coupled eigenmode. The output spectrum for the d_z=1.50mm 2D PSL presented in Fig.15 shows the eigenmode at 75GHz and the spatial harmonic (with an acceptably low level) around 150GHz. These results confirm that the theory and simulations are scalable in frequency and that the mode selection can be

maintained as the transverse cavity size is increased.

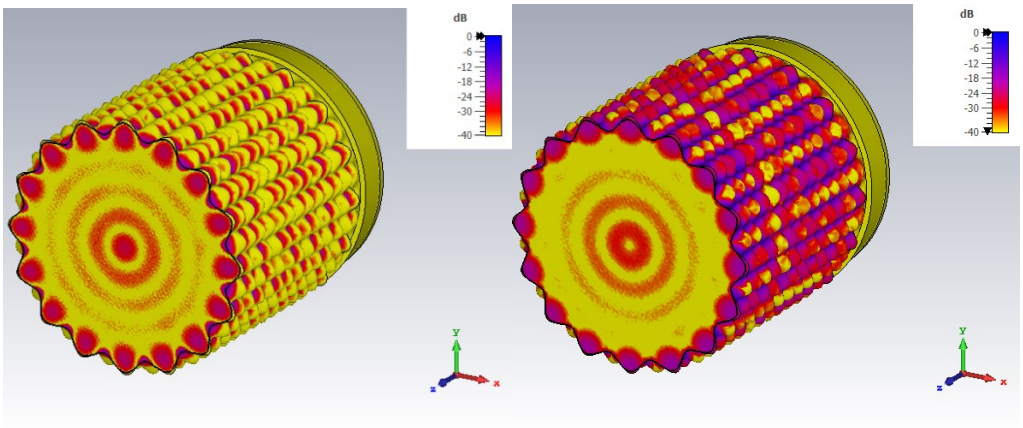

Fig. 14. Contour plots showing the axial electric (left) and tangential magnetic (right) field components in the center of an overmoded, D/λ=5 2D PSL.

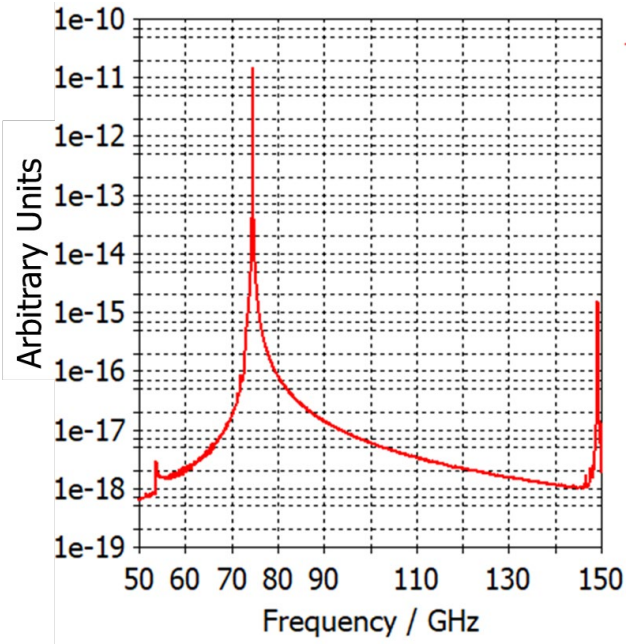

Fig. 15. Output spectrum for 75GHz 2D PSL with axial period, dz=1.50mm and mean radius, 10mm.

5. Cylindrical periodic surface lattice experiments

Numerical simulations have been carried out at various frequencies including 35 GHz, 75 GHz, 94 GHz, 140 GHz, 200 GHz, 350 GHz and 395 GHz with the detailed examples of simulation results 350 GHz reported above. Laboratory experiments at any of these frequencies are now feasible. For the forthcoming laboratory experiment a source operating in the W-band (75 -110 GHz) has been designed. Two-dimensional PSL interaction structures have been constructed using electrochemical deposition of copper on a cylindrical aluminum former with the aluminum subsequently removed by dissolving in strong alkali solution The machined aluminum former is shown in Fig. 16 and the outside of the electrochemically deposited copper structure is shown in Fig. 17.

A sharpened annular graphite cathode is used to provide the annular electron beam source. The electron beam of ~100ns pulse duration that can be varied over the

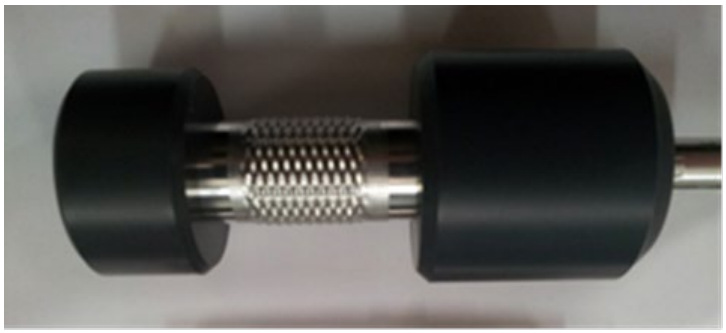

Fig. 16. **Machined aluminum former.**

accelerating voltage range from 60 kV to 80 kV, is guided by a strong axial magnetic field provided by a superconducting magnet and is passed through the cylindrical periodically structured copper cavity. The superconducting magnet is one that has been used in other applications and is capable of supplying a magnetic field that can be systematically varied up to 11 tesla, although the magnetic field needed to provide electron beam transport

through the cylindrical 2D PSL structure in the present experimental program is actually only a few tesla. The diagnostics available to characterize the electron beam include Faraday cup, witness plate and macroscopic current/voltage measurements. The mm-wave diagnostics include cut-off waveguide filters, W-band heterodyne mixer and intermediate frequency capture and analysis, as well as output mode pattern measurements. The assembled W-band oscillator is shown in Fig. 18. More than one 2D PSL interaction structure has been constructed, so as to be able to change the structure and compare the experimental results with numerical simulations carried out for a range of structure parameters. In order to be able to easily change the 2D PSL structure the vacuum envelope of the oscillator, including the electron gun, the output waveguide, electron beam collector and the output window have been constructed so as to be demountable. The vacuum system is continually pumped and the measured vacuum pressure is ~10^{-6} mb. This pressure is sufficiently low to allow reliable production from the sharpened graphite cold cathode of ~100 ns electron beam pulses.

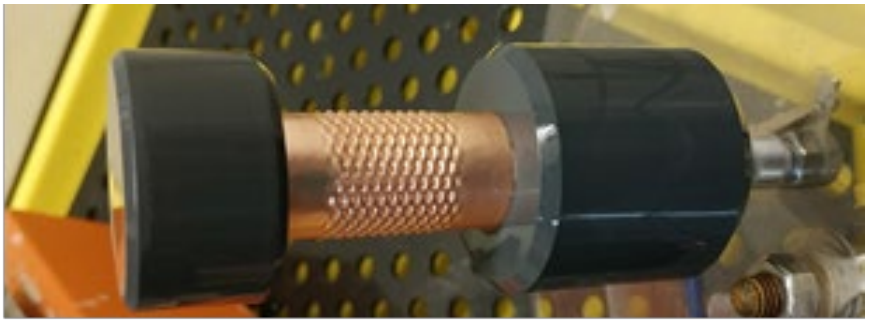

Fig.17. Electrodeposited copper 2D cylindrical periodic structure.

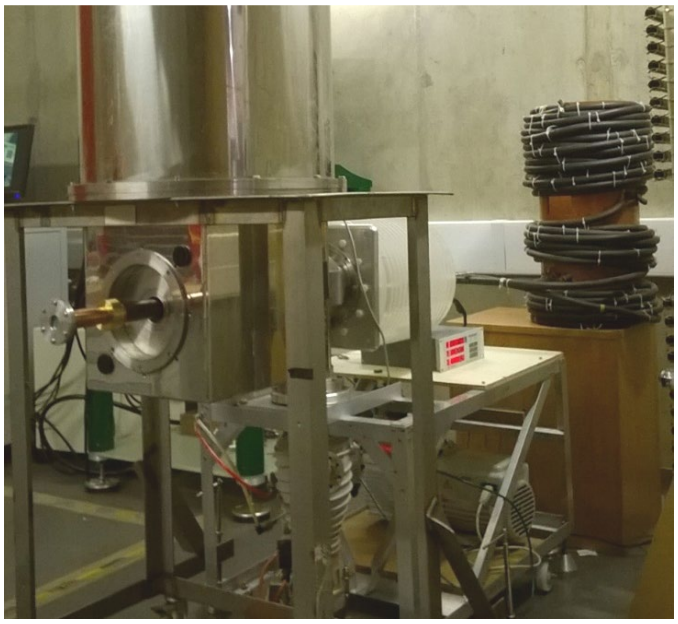

Fig.18. Assembled oversized W-band 2D periodic lattice oscillator.

6. Conclusions

The theory and numerical simulations carried out during this research project have advanced the understanding of two-dimensional periodic structures in cylindrical geometry. As a consequence there are good prospects for achieving improved high power mm-wave radiation sources using these novel structures with the eventual aim of increasing the diameter to wavelength ratio. The novel high order mode coupling method presented in this paper is applicable even to extremely overmoded cavities and D/λ values of 100 are theoretically possible. The new electron beam driven W-band mm-wave source has been designed and constructed based on the principles presented in this report.

An overmoded cylindrical Two Dimensional Periodic Surface Lattice (2D PSL) composed of a metallic low contrast surface lattice which can be considered as a high-impedance surface and approximated as a cylindrical waveguide partially loaded with a meta-

dielectric material, has been studied, fabricated and assembled within a 100 GHz oscillator. This 2D PSL has been shown to facilitate the efficient Cherenkov interaction between a high energy electron beam and a highly overmoded cavity, which conventionally would produce a highly inefficient interaction. The success of this device is attributed to the coupling of volume and surface modes, and resultant coupled cavity eigenmode formation, which provides mode selection within the oversized structure. In addition to the major step up in maximum power capability enabled by the efficient mode selection process in the oversized cavity, additional benefits result from creating a meta-dielectric using a metallic periodic structure on the inner wall of the cavity (i) a Cherenkov interaction is enabled by the physical properties of the meta-dielectric (ii) the usual disadvantage of charge accumulation on a conventional insulating dielectric is eliminated, since the periodic structure consists of a metallic electrical conductor (iii) optimal cooling is enabled by the location of the periodic structure on the thermally conducting metallic wall of the cavity.

Recent results at 350GHz show the potential to achieve 1.95 MW output power with 24% electronic efficiency despite the relatively high ohmic losses associated with high frequencies. The proposed 2D PSL oscillators have the added benefit of requiring a relatively modest 1.5-3T magnetic field to transport the electrons through the 2D PSL cavity, allowing for convenient deployment in applications. Simulations confirm that the device operates reasonably efficiently at voltages and currents as low as 30kV and 20A. The simulated planar cathode and grid configuration, leading to the generation of a high

quality, thin annular beam, can be reproduced, by constructing carbon nanotube cathodes, suitable for pulsed sources.

The theory and modeling are scalable to different frequencies, and also show the potential for the parameters of the 2D PSL sources to be tuned for different operating regimes increasing the broad scope of this research. The theory and simulation of powerful, pulsed 2D PSL oscillators with $D/\lambda=3.5$ and $D/\lambda=5$ have stimulated fresh ideas for further research.

7. Future Research Opportunities

Numerical modeling has shown the potential for powerful radiation output at different frequencies confirming the scalability of the PSL structures. Building on the success of this research, an exciting possibility is to design and implement a novel carbon nanotube (CNT) cathode to produce a high quality beam inherent to the successful operation of the device. Working in parallel and in synergy with ongoing AFOSR research within the Atoms, Beams and Plasmas group at the University of Strathclyde, we envisage the potential to utilize tested and proven CNTs to construct a suitable cathode.

Obtaining a high quality electron beam will stimulate further research possibilities including the realization of superradiance within CNT 2D PSL devices which can then be developed to phase lock an array of N 2D PSLs for exceptionally powerful, focused

radiation. Although phase-locking 1D backward wave oscillators (BWOs) has been recently achieved at Ka-band, neither phase-locking superradiant 2D PSLs, nor incorporating a CNT film cathode within a 2D PSL device, have yet been accomplished. Moreover, based on the success of this present research, we foresee the potential to synchronize W-band, CNT 2D PSLs to within 2.5 picoseconds, to achieve several "world firsts".

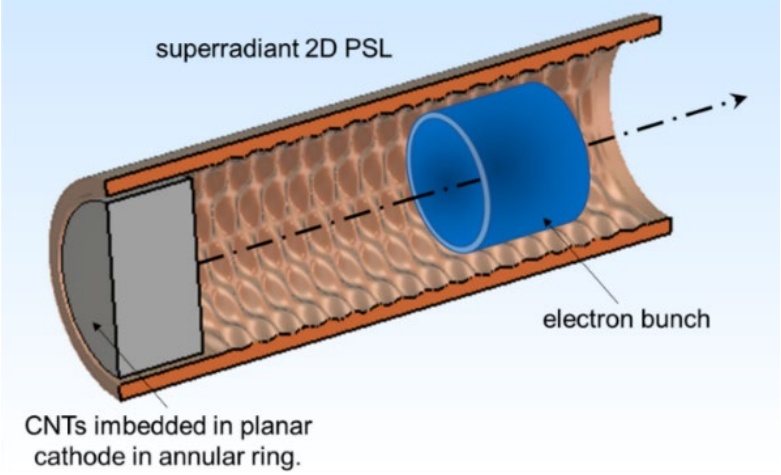

Fig. 19. Diagram showing concept of superradiance in 2D PSL with CNT cathode.

To achieve superradiance, the gain must be so high that a very short pulse of electrons produces a short pulse of very high power electromagnetic radiation. Since no modeling or experimental measurements for an overmoded superradiant 2D PSL source with CNT cathodes have been made worldwide, it remains to be discovered how low the voltage can be reduced while retaining high output power. Recent simulations indicate that the electron beam can be transported through the interaction cavity using a relatively low applied magnetic field (~1.5T) and it is yet to be established how low this magnetic field can eventually be made.

The power flux per unit area, or the magnitude of the Poynting vector, at the output

window of 9 mm radius from a single W-band superradiant 150 MW, 2D PSL source is estimated to be $\sim 5 \times 10^{11}$ Wm^{-2} and for a pair of phase synchronized 2D PSL sources, the peak magnitude of the Poynting vector in the far-field, because of the coherent co-operative interference of the two beams, will be equivalent to the peak power flux density produced by four superradiant 2D PSL sources of 150 MW each. Then scaling of N such sources to be equivalent in their peak magnitude of power flux density to N^2 sources logically follows. Simultaneously increasing D/λ towards 10 will further increase the potential power of an array of 2D PSLs, and **many 10's of GigaWatts** of output power can be extrapolated, with applications including radar, directed energy and power beaming.

In addition to backward wave interactions, recent theoretical and analytical dispersion studies have shown the potential for the 2D PSLs to support pi-mode and forward wave interactions, uncovering interesting new source and amplifier possibilities. Exploring these different interactions, and investigating the viability of devices based on forward wave interactions, could eventually lead to the development of powerful, 2D PSL amplifiers based on a forward wave-beam interaction. This could be further explored as an alternative route to phase-locking whereby two or more 2D PSLs could be synchronized using forward wave amplification by designing narrow band 2D PSL amplifiers. Using this method, the synchronization would require an identical signal to be fed into the input of the individual amplifiers and these amplifiers would need to be sufficiently phase stable in their amplification.

8. Research staff

Dr. Amy J. MacLachlan is the Research Associate employed by this grant and has worked on this research project throughout the period of this report.

9. Publications

Publications 2017-22

1. MacLachlan, A.J, Phipps, A.R., Robertson, C.W., Konoplev, I.V., Cross, A. W.and Phelps, A.D.R., Surface and volume mode coupling experiments for high power mm-wave sources, IEEE ed, pp. 61-63, 2017. DOI: 10.1109/UCMMT.2016.7873961

2. Phipps, A.R., MacLachlan, A.J., Robertson, C. W., Cross, A.W. and Phelps, A.D.R., Additive manufacturing method of prototyping novel mm-wave and THz sources, IEEE ed.. pp. 238-240, 2017. DOI: 10.1109/UCMMT.2016.7874023

3. Phipps, A.R., MacLachlan, A. J., Robertson, C. W., Zhang, L., Konoplev, I. V., Cross, A. W. and Phelps, A. D. R., Electron beam excitation of coherent sub-terahertz radiation in periodic structures manufactured by 3D printing, Nuclear Instruments and Methods in Physics Research Section B: Beam Interactions with Materials and Atoms, NIMB, vol. 402, pp. 202-205, 2017.

4. MacLachlan, A.J., Phipps, A. R., Robertson, C. W., Konoplev, I. V., Ronald, K., Cross, A. W. and Phelps, A. D. R, Millimeter-wave periodic surface lattices for mode control in vacuum electronic sources, IEEE, 18th IVEC conference, London, 2017. UK, DOI: 10.1109/IVEC.2017.8289679

5. MacLachlan, A.J., Robertson, C.W., Cross, A.W. and Phelps, A.D.R., Volume and surface mode coupling experiments in periodic surface structures for use in mm-THz high power radiation sources, AIP Advances, vol. 8, no. 10, Article 105115, 2018. DOI: 10.1063/1.5020542

6. MacLachlan, A.J., Robertson, C.W., Konoplev, I.V., Cross, A.W., Phelps, A.D.R., and Ronald, K., Resonant excitation of volume and surface fields on complex electrodynamic surfaces. Phys. Rev. Appl., 11, 034034, (2019).

7. MacLachlan, A.J., Robertson, C.W., Ronald, K., Cross, A.W., and Phelps, A.D.R., Mode coupling in periodic surface lattice and metamaterial structures for mm-wave and THz applications. Springer Nature, SN Applied Sciences, 6, 613, (2019).

8. Cross, A.W., MacLachlan, A.J., Robertson, C.W., Zhang, L., Donaldson, C.R., Yin, H., Phelps, A.D.R, and Ronald K., Oversized W-band 2D periodic lattice oscillator,

In: IEEE, International Vacuum Electronics Conference, (IVEC 2019), Busan, Korea, 28 April -1 May 2019, (2019).

9. Whyte, C.G., MacLachlan, A.J., Robertson, C.W., Cross, A.W., Zhang, L., Donaldson, C.R., Phelps , A.D.R, and Ronald, K. ,W-band 2D periodic lattice oscillator, IEEE Pulsed Power and Plasma Science Conference 2019 (PPPS/ICOPS 2019), Orlando, USA, 23-28 June 2019, (2019).

10. Cross, A.W., MacLachlan, A.J., Robertson, C.W., Zhang, L., Ronald K., and Phelps A.D.R., Highly Overmoded MM-wave Oscillator Experiments, In: 12th UK-Europe-China Workshop on Millimetre Waves and THz Technologies, (UCMMT 2019), London, UK, 20-22 August, 2019, (2019).

11. MacLachlan, A.J., Robertson, C.W., Cross, A.W., Ronald, K., and Phelps, A.D.R. Volume and surface field coupling on complex electrodynamic surfaces for MM-wave and THz applications. In: 12th UK-Europe-China Workshop on Millimetre Waves and THz Technologies, (UCMMT 2019), London, UK, 20-22 August, 2019, (2019).

12. MacLachlan, A.J., Robertson, C.W., Cross, A.W., Ronald, K., and Phelps A.D.R., Excitation and Coupling of Volume and Surface Fields on Complex Electrodynamic Surfaces at Mm-wave and THz Frequencies, IET Microwaves, Antennas and Propagation, 14, (11), 1151-1156, 2020, (2020).

13. MacLachlan, A.J., Robertson, C.W., Cross, A.W., Ronald, K., Phelps, A.D.R., Powerful, over-moded 0.14 THz radiation source, 45th International Conference on Infrared, Millimeter and Terahertz Waves (IRMMW-THz 2020), Buffalo, NY, USA, 8-13 November, 2020. [Paper presented remotely], (2020).

14. MacLachlan, A.J., Robertson, C.W., Cross, A.W., Ronald, K., Phelps, A.D.R., Overmoded, high-power 0.2THz radiation source based on a cylindrical 2D Periodic Surface Lattice cavity, International Conference on Plasma Science (ICOPS 2020), Singapore, 6-10 December, 2020. [Paper presented remotely], (2020).

15. MacLachlan, A.J., Robertson, C.W., Cross, A.W., Ronald, K., Phelps, A.D.R., Powerful radiation source at 0.35 THz based on overmoded, periodic cavities, 22nd International Vacuum Electronics Conference, (IVEC 2021), ESA-ESTEC, The Netherlands, 27-30 April 2021 [Paper presented remotely], (2021).

16. MacLachlan, A.J., Robertson, C.W., Cross, A.W., Phelps, A.D.R., 0.395 THz Surface Wave Oscillator for DNP-NMR Applications, 14th UK-Europe-China Workshop on Millimetre Waves and THz Technologies (UCMMT 2021), Lancaster, United Kingdom, 13-15 September 2021 [Paper presented remotely], (2021).

17. MacLachlan, A.J., Robertson, C.W., Phelps, A.D.R., Cross, A.W., 'Concept and modeling of an efficient, high power, 0.35 THz source', The 48th IEEE International

Conference on Plasma Science (ICOPS 2021), Lake Tahoe, United States, 12-16 September 2021 [Paper presented remotely], (2021).

18. MacLachlan, A.J., Robertson, C.W., Cross, A.W., Phelps, A.D.R., Efficient, 0.35 THz Overmoded Oscillator Based on a Two-Dimensional Periodic Surface Lattice', IEEE Trans. Electron. Dev. (submitted for publication), May 2022.

10. Professional Activities

Conference and society committees and awards (2017-2022):

Co-investigator: Adrian Cross:
Cockcroft Institute Management Committee, 2017-2022
Organizing Committee (Treasurer) of European Microwave Week (three conferences and one exhibition), Excel Centre, London, UK, 13-18 February 2022

Principal Investigator: Alan Phelps:
Received the IEEE Plasma Science and Applications (PSAC) Award in 2017
Organizing Committee (Treasurer) for ESCAMPIG Conference, Glasgow, 2018
International Committee, IEEE ICOPS Conference, Denver, USA, 2018
Elected HPEM Fellow of the Summa Foundation, 2018
Co-chair of International Advisory Committee, UCMMT annual international conferences held in 2017, 2018, 2019, 2020 and 2021
Appointed 'Emeritus Professor', University of Strathclyde, from 1st October 2022

11. Appendices

A1. Grant Award FA9550-17-1-0095 Modification No. P00004

A2. SF298 Report Documentation Page

APPENDIX A1

Grant/Cooperative Agreement Modification

1. AWARD NO.	2. MODIFICATION NO.	3. EFFECTIVE DATE	4. PURCHASE REQUEST NO.	PAGE OF
FA9550-17-1-0095	P00004	29 MAR 2021	See Block 9	1 2

5. ISSUE BY AFRL/RBKR2 CODE FA9550
USAF, AFRL DUNS 143574726
AF OFFICE OF SCIENTIFIC RESEARCH
875 NORTH RANDOLPH STREET, RM 3112
ARLINGTON VA 22203-1954
EMILY R. BANNAN +44 (0)1895616041
emily.bannan@us.af.mil

6. AWARDED TO CAGE CODE KD0L4
UNIVERSITY OF STRATHCLYDE VIZ ROYAL
COLLEGE OF SCIENCE
SCOTTISH LOCAL AUTHORITIES MANAGEMENT
CENTRE
16 RICHMOND STREET
GLASGOW G1 1XT UNITED KINGDOM

9. ALLOCATED FUNDING: The following funds with associated Accounting Classification reference number(s) (ACRNs) are allotted to this agreement:

ACRN	FUND CITATION(s)	AMOUNT

FOREIGN GRANT

SPECIAL INSTRUCTIONS: N/A
PAYING OFFICE INSTRUCTIONS: N/A
PAYMENT SCHEDULE (if applicable): N/A

10. FUNDING HISTORY:	Government Share	11. Recipient Share	12. Total
Previously Obligated:	$200,000.00	$0.00	$200,000.00
Obligated by this Action:	$0.00	$0.00	$0.00
Total Obligated to date:	$200,000.00	$0.00	$200,000.00
13.TOTAL AWARD AMOUNT CHANGE	$0.00	$0.00	$0.00

14. DESCRIPTION OF MODIFICATION

The purpose of this modification is to extend the period of performance through 14 Apr 2022. The reporting requirements are revised as shown on page 2.

All other terms and conditions remain unchanged as a result of this modification.

RESEARCH TITLE: "Advanced surface artificial materials for high power microwave sources"
PI: Prof. Alan Phelps
PO: Dr. Nathaniel Lockwood

FOR THE RECIPIENT		FOR THE UNITED STATES OF AMERICA	
15. SIGNATURE		16. SIGNATURE	
17. NAME AND TITLE	18. DATE SIGNED	19. NAME AND TITLE EMILY R. BANNAN GRANTS OFFICER	20. DATE SIGNED 29 Mar 2021

ConWrite Version 7.4.0.0
Created 29 Mar 2021 6:54 AM

The Reports are hereby changed:

Reports are due on or before the following dates. Submit all reports to AFRL.EOARD.TechReports@us.af.mil

TYPE OF REPORT	DUE DATE
Annual Performance Report	14 APR 2018
Annual Performance Report	14 APR 2019
Annual Performance Report	14 APR 2020
Annual Performance Report	14 APR 2021
Final Performance Report, Including SF298 Report Documentation Page	13 JUN 2022
Final Invention Report (DD Form 882)	13 JUN 2022
Final SF 425 Federal Financial Report, Including Line 11	13 JUN 2022
Quarterly SF 425 Federal Financial Report	*below

* SF 425 Quarterly Federal Financial Reports are required because payment has been made by advance. These reports are due in accordance with the dollar threshold of your respective award.

Dollar threshold and reporting are as follows (your report will be done according to the item in bold print):

Awards greater than $1,000,000 reports will be due quarterly
Awards between $500,000 and $999,999 reports are due semi - annually
Awards less than $500,000 reports will be due annually

APPENDIX A2

REPORT DOCUMENTATION PAGE

1. REPORT DATE	2. REPORT TYPE	3. DATES COVERED	
		START DATE	END DATE
31-05-2022	Final	15-04-2017	14-04-2022

4. TITLE AND SUBTITLE

Advanced Surface Artificial Materials for High Power Microwave Sources

5a. CONTRACT NUMBER	5b. GRANT NUMBER	5c. PROGRAM ELEMENT NUMBER
	FA9550-17-1-0095	
5d. PROJECT NUMBER	**5e. TASK NUMBER**	**5f. WORK UNIT NUMBER**

6. AUTHOR(S)

MacLachlan, Amy, J., Cross, Adrian, W., Phelps, Alan, D. R.

7. PERFORMING ORGANIZATION NAME(S) AND ADDRESS(ES)

UNIVERSITY OF STRATHCLYDE
16 RICHMOND STREET
GLASGOW G1 1XT
UNITED KINGDOM

8. PERFORMING ORGANIZATION REPORT NUMBER

9. SPONSORING/MONITORING AGENCY NAME(S) AND ADDRESS(ES)	10. SPONSOR/MONITOR'S ACRONYM(S)	11. SPONSOR/MONITOR'S REPORT NUMBER(S)
EUROPEAN OFFICE OF AEROSPACE RESEARCH AND DEVELOPMENT (EOARD) 86 BLENHEIM CRESCENT RUISLIP MIDDLESEX HA47HB UNITED KINGDOM	AFOSR IOE	

12. DISTRIBUTION/AVAILABILITY STATEMENT

A DISTRIBUTION UNLIMITED: PB Public Release

13. SUPPLEMENTARY NOTES

14. ABSTRACT

Research results are reported of advanced cylindrical surface two-dimensional periodic surface lattice (2D PSL) structures for applications in high power microwave sources. 2D PSL structures enable highly overmoded sources to emit coherently at higher powers than conventional sources. The principle is independent of frequency from a few GHz up to THz frequencies. This research has produced several publications. Analytical theory, combined with numerical modeling, has revealed several very promising new research routes. Recent results have highlighted the potential for higher performance 2D PSL sources using electron beams produced by advanced carbon nanotube cathodes. Exciting new research opportunities include phase locking of multiple 2D PSL oscillators, achieving superradiant 2D PSL sources and exploring the potential for powerful 2D PSL amplifiers. Accomplishing these goals would deliver "world firsts" and produce record output power levels.

15. SUBJECT TERMS

High power microwaves, millimeter-waves, vacuum electronics, periodic surface lattices, metadielectrics, Cherenkov microwave sources.

16. SECURITY CLASSIFICATION OF:			17. LIMITATION OF ABSTRACT	18. NUMBER OF PAGES
a. REPORT	b. ABSTRACT	C. THIS PAGE		
U	U	U	UU	40

19a. NAME OF RESPONSIBLE PERSON	19b. PHONE NUMBER *(Include area code)*
Lockwood, Nathaniel	011-44-1895-616005

PREVIOUS EDITION IS OBSOLETE.

STANDARD FORM 298 (REV. 5/2020)
Prescribed by ANSI Std. Z39.18